HHS Public Access

Author manuscript

Magn Reson Med. Author manuscript; available in PMC 2014 September 04.

Published in final edited form as:

Magn Reson Med. 2014 February ; 71(2): 797–806. doi:10.1002/mrm.24695.

Respiration Based Steering for High Intensity Focused Ultrasound Liver Ablation

Andrew B. Holbrook[1], **Pejman Ghanouni**[1], **Juan M. Santos**[2], **Charles Dumoulin**[3], **Yoav Medan**[4], and **Kim Butts Pauly**[1]

[1]Department of Radiology, Stanford University, Stanford, California

[2]HeartVista, Inc., Palo Alto, California

[3]Department of Radiology, Cincinnati Children's Hospital Medical Center, Cincinnati, Ohio

[4]Department of BioMedical Engineering, Technion, Israel

Abstract

Purpose—Respiratory motion makes hepatic ablation using high intensity focused ultrasound challenging. Previous HIFU liver treatment had required apnea induced during general anesthesia. We describe and test a system that allows treatment of the liver in the presence of breathing motion.

Materials—Mapping a signal from an external respiratory bellow to treatment locations within the liver allows the ultrasound transducer to be steered in real time to the target location. Using a moving phantom, three metrics were used to compare static, steered, and unsteered sonications: the area of sonications once a temperature rise of 15°C was achieved, the energy deposition required to reach that temperature, and the average rate of temperature rise during the first 10 seconds of sonication. Steered HIFU in vivo ablations of the porcine liver were also performed and compared to breath-hold ablations.

Results—For the last phantom metric, all groups were found to be statistically significantly different ($p \leq 0.003$). However, in the other two metrics, the static and unsteered sonications were not statistically different ($p > 0.9999$). Steered in vivo HIFU ablations were not statistically significantly different from ablations during breath-holding.

Conclusions—A system for performing HIFU steering during ablation of the liver with breathing motion is presented and shown to achieve results equivalent to ablation performed with breath-holding.

Keywords

HIFU in the liver; HIFU beam steering; real time MRI

Correspondence to: Andrew B. Holbrook, The Lucas Center for Magnetic Resonance Imaging 1201 Welch Road, Stanford, CA, 94305, Phone: (650) 469-3853, Fax: (650) 723-5795, aholbrook@stanford.edu.

Introduction

MR-guided high intensity focused ultrasound (HIFU) ablation has shown great potential for noninvasive treatments throughout the body. Ultrasound energy is focused through soft tissue to a target, where energy deposition results in thermal ablation of the lesion. HIFU therapy has been successfully delivered clinically to many tissue types, including the uterus [1], prostate [2], brain [3,4], bone [5], pancreas [6], and liver [7,8].

Clinical HIFU treatments of the liver have been performed, but required apnea induced during general anesthesia to limit respiratory motion during tumor targeting, using ultrasound transducers that were limited because they were fixed to the MR table [7]. However, techniques suitable during free breathing are desired in order to make the procedure less invasive. Focused ultrasound treatment of the liver during free breathing is challenging because the ultrasound focus must be maintained on the desired target to accrue sufficient thermal dose. A poorly maintained focus in a highly perfused organ such as the liver can mean the focus will not achieve enough thermal dose to achieve coagulative necrosis. Further requirements are that the imaging and thermometry processing methods accurately depict the temperature rise. Lastly, these elements must be put together into a complete system that is designed for this purpose, with scan prescription, location verification, motion monitoring, beam steering, and temperature monitoring.

For several HIFU systems, the HIFU transducer is embedded inside an MR table and its position is either immobilized or robotically controlled. With the transducer location always set, the system can focus purely on target tracking. As such, several real time approaches have been presented to tracking of the liver [9] or its vessels [10] in real time. These approaches can be accelerated to fast speeds with parallel imaging and faster processing (ie. with Graphical Processing Units (GPUs) [11]) to decrease system latency and allow moving volumetric organ ablation, as demonstrated by Quesson et al [12]. Respiratory gating has also been used for HIFU liver ablation, even transcostally by Auboiroux et al [13].

Ultrasound transducer systems external to the MR table allow the transducer to be strapped into place anywhere along the patient, providing added flexibility for tumor targeting. With these movable devices, the transducer position and orientation on the patient may vary with respiration. Therefore, in order to ablate successfully with such a transducer-target arrangement, the location of both the transducer and target must be tracked in real time. Our approach is to steer the beam in the presence of both liver and transducer motion. Immediately prior to the treatment, tissue and transducer motion during the respiratory cycle are measured and the positions are stored in a lookup table, which is then accessed in real time. During treatment, the beam is steered appropriately and with low latency.

In this work, by combining respiratory based steering into an integrated MR HIFU system, we achieve hepatic ablation in the presence of breathing motion, as a step toward HIFU treatment with free breathing. Steering accuracy was quantitatively assessed through a series of phantom and *in vivo* porcine liver experiments.

Methods

System Setup

All experiments were performed with a 3.0T Signa Excite (GE Healthcare, Waukesha WI) in conjunction with an ExAblate Conformal Bone System (InSightec, Ltd, Tirat Carmel, Israel). The ExAblate system features an extracorporeal, strappable phased array transducer with 1000 elements, a center frequency of 550 kHz, and a maximum acoustic power of 150 Watts. The system is capable of performing real time steering, with the ability to switch rapidly between various pre-allocated phase tables within 16 ms. The overall amplitude or power applied to these elements could be varied too, although only on the global level and not element by element. The device also contains four coils for active MR tracking.

All MRI scanning was performed with the RTHawk (HeartVista, Inc, Palo Alto CA) real time MRI system [14]. A respiratory pressure belt connected to the scanner was used for respiratory measurements for all experiments. A real time MRI interface for HIFU liver ablation was designed for controlling the scanning and reconstructing the images, as shown in Figure 1. The interface was capable of receiving and displaying various types of data, including signals from MR tracking coils, image reconstructions (magnitude, coil localization, thermometry, acoustic radiation force (ARFI)), and data from peripheral systems such as the respiratory belt and the InSightec transducer via Transmission Control Protocol (TCP) and User Datagram Protocol (UDP) network protocols. The interface was written in C++, using a 22” M2256PW (3M Touch, Methuen, MA) multi-touch monitor for various touch interactions, ranging from controlling MR scans, prescribing HIFU treatments, and performing analysis of image data. For these experiments, RTHawk was configured to receive data from four sequences: a GRE scout sequence, an MR-thermometry sequence, an MR acoustic radiation force sequence (MR-ARFI), and an MR-tracking sequence. The following sections describe the workflow steps in more detail.

Scout Collection

Ungated gradient recalled echo scout images (30 × 30 cm field of view, 2.34 × 2.34 mm acquired resolution, 4.7mm slice thickness, flip angle: 30° (user selectable), TE = 1.7 ms, TR = 7 ms, 60% partial k-space coverage, 125 kHz BW, 537 ms per frame) were collected throughout the volume. More scout images could be collected by the user as desired in the axial, sagittal, and coronal planes. Additionally, scout images could be collected parallel and perpendicular to the transducer face, once the transducer location had been initialized.

Transducer Tracking

The ExAblate Conformal Bone System is equipped with four active MR-tracking coils to allow for localization within the magnet. A phase-dithered Hadamard MR tracking sequence [15] with 6 dithers was used to determine the tracking coil locations. The maximum signal in each Hadamard direction was used to determine the position of each coil. This location was then gradient warping compensated, and, by principal component analysis, the location of the transducer was determined. Principal component analysis determined the normal direction and the center of the transducer face. As the distance was known from each element to the center of the transducer face, the location of the individual elements on the

transducer could be calculated. With this sequence, the transducer location could be calculated at each respiratory phase. The position of the transducer and liver were used to calculate a targeting table, as described below. Given the transducer position, the potential treatment area was annotated by a color overlay on the GRE scout images, as shown in Figure 2. This consists of a region 5 to 15 cm from the face of the transducer, at a steering angle of less than 30 degrees. The transducer treatment zone location is readjusted on the displayed images each time the transducer's position is sampled.

Liver Tracking

Fiducial marker tracking was performed via collection of a series of single slice gradient recalled echo images (30 × 30 cm field of view, 2.34 × 2.34 mm acquired resolution, 4.7 mm slice thickness, flip angle: 30° (user selectable), TE = 1.7 ms, TR = 7 ms, 60% partial k-space coverage, 125 kHz BW, 537 ms per frame) at multiple respiratory phases. Scans were collected throughout the respiratory cycle: 10 equally spaced phases during inspiration and 10 during exhalation. From these images, fiducial markers could be placed on two types of features: boundaries such as the diaphragm and bright objects such as through-plane blood vessels. Initially, the user marks either type of fiducial marker in one of the respiratory phase images. As these are 2D representations of motion, they were typically marked in tracking images acquired in the sagittal plane, where out-of-plane motion is minimized [16]. Next, the fiducial markers are identified in the two images adjacent in respiratory phase to this one. This is performed by creating an edge image for the diaphragm marker and by finding the maximum location along the respiration direction, and for the vessel marker by finding the maximum pixel within a 2 cm by 2 cm frame centered around the most recently selected point. The process continues until the fiducial marker has been identified in all images.

Respiration-based beam steering

With the fiducial markers positioned, a target is defined within this overlaid region on a single image of the set. The target can then be adjusted on each of the remaining images, based on the motion of the fiducial markers over the same period. With the transducer location, liver position, and target position determined at each respiratory phase, a lookup table is created for the transducer phases at each point in the respiratory cycle. This lookup table was used in two modes: calibration mode or ablation mode. During calibration mode, the transducer phases for a particular respiratory phase location were loaded into the transducer. As the respiratory signal entered that particular respiratory phase, the MRI and ultrasound could be triggered to immediately power on for an acoustic radiation force measurement during a single TR of the calibration MR-ARFI sequence. This acquisition will be described in the next section on focal spot calibration. During ablation mode, the transducer is continuously on. As the respiratory signal enters a respiratory phase, the transducer switches its phase profile to the appropriate one based on the lookup table. This is discussed in greater detail in the subsequent Steered Ablation section.

Focal Spot Calibration

Prior to HIFU treatment, targeting verification was performed with MR acoustic radiation force imaging. MR-ARFI images at various respiratory motion locations were acquired with two single-shot acquisitions (8 × 20 cm field of view, 1.40 × 1.40 mm acquired resolution,

zero-filled to achieve a pixel size of 0.81 × 0.81 mm, TE=74.5 ms, TR at least 2000 ms, 70.2 ms echo train length (1.24 ms echo spacing), 65% partial k-space coverage, 6.8 mm slice thickness (FWHM of refocusing pulse slice profile)), where the displacement encoding gradients were inverted for the second shot [17]. The actual MR-ARFI displacement was compared to the desired target location, and if the two were not in alignment, calibration was performed by indicating the correct position via interacting with the touch screen or using the mouse. The ARFI scan was retaken to verify that calibration had been achieved.

Thermometry

A hybrid multibaseline/referenceless thermometry algorithm was used to calculate thermometry images in these experiments [18]. The pulse sequence utilized was a 3 shot readout segmented EPI sequence (8 × 20 cm, 1.40 × 1.40 mm acquired resolution, zero-filled to achieve a pixel size of 0.81 × 0.81 mm, BW = 9kHz, TE = 15.9 ms with 57 echoes (1.13 ms echo spacing), TR = 117 ms with a readout time of 64 ms (351 ms per image, 65% partial k-space coverage, 4.7 mm slice thickness with a 1–2-1 water selective spatial spectral binomial pulse). The pulse sequence utilized outer volume suppression via a series of high bandwidth polynomial-phase RF saturation bands to reduce the field of view in the phase encode direction. Furthermore, the pulse sequence was shown in the past to measure temperature reliably, even in moving organs like the liver, as described previously [19]. Prior to ablation, a series of baseline images was acquired throughout the respiratory cycle to form a multibaseline library. During the ablation, the acquired magnitude images are compared to the baseline library, with the best fit selected by magnitude correlation. Once the baseline image phase is subtracted, an l_2 referenceless thermometry reconstruction is performed on the phase subtracted image. The reconstruction is performed within user defined ROIs in the image, which are also tracked to follow motion. A single thermometry slice was run at a time. However, this slice was often moved to other locations on request to assess temperature rises in other locations. Baseline libraries for each slice location would be collected prior to ablation.

Steered Ablation

Sonication proceeded after the lookup table was created, the target location was verified, and the thermometry baseline was acquired. The transducer power was controlled with the multi-touch interface, instantly scaling the power between 0 and its maximum when requested. The focal spot location could be switched between one of 32 different locations. As the respiratory belt was sampled, the respiratory phase value was determined. From this, the location within the target location table was selected. If the target location was different from the current ablation location, the new value was immediately sent via UDP to the PC directly controlling the transducer, and the change was made. This procedure would repeat until the operator reduced the power to 0.

Phantom Experiments

To validate respiration-based steering, a polyacrylamide gel phantom was placed inside a degassed water filled container inside the magnet. The HIFU transducer was placed underneath the container and fixed to the table. Degassed water was initially used to couple the transducer membrane to the container; afterwards the membrane itself leaks water to

keep the membrane coupled to the container. The gel phantom was attached to an arm which was attached to a servomotor placed outside the magnet bore and moved back and forth within the water filled bucket, as shown in Figure 3. The respiratory belt was attached to a fixed position on the table. As the stage moved in and out, the respiratory belt lengthened and shortened, simulating breathing.

The motor pushed the phantom back and forth inside the container with an amplitude of approximately 1.5 cm peak-to-peak, controlled by a software script running in E-Prime (Psychology Software Tools, Inc., Sharpburg, PA). The phantom repeatedly moved back and forth sinusoidally at a maximum speed of 10.4 mm/s. A cycle took approximately 4.5 seconds. The respiratory belt signal was sampled every 25 ms and connected via serial port to the computer running RTHawk and the custom liver user interface.

Ungated scout images were first acquired of the phantom. A slice parallel to the transducer face at roughly the midpoint of the phantom was selected for sonication monitoring. At this slice, gated scout images were acquired for each phase of the phantom's motion. Additionally, throughout all phases of the phantom motion, the position of the transducer's orientation was determined (although, in these experiments the transducer's location was fixed to the table).

HIFU sonications were performed at a constant power of 74 acoustic Watts, targeting the center of the phantom. Three types of sonications were performed, as depicted schematically in Figure 4. The first was a standard sonication with no motion, i.e. the servomotor was turned off. A single location was targeted and no steering was required. The second type of sonication, the middle example of Figure 4, was a sonication with the described motion. A single location was targeted in the first phase image of the imaging slice, and despite the fact that the phantom moved, the transducer's focus remains fixed at this position (no steering). The final phantom sonication, the right example of Figure 4, was a sonication with the described motion and transducer focus steering. The phantom's motion cycle was found from the images with the diaphragm method, marking the upper edge of the phantom. Vessel fiducial markers were not utilized, as this was a homogeneous gel phantom. During the sonication, the respiratory belt signal was monitored, and as the value was predicted to enter a new respiratory phase, the transducer phases were changed in order to move the focal position accordingly. The focal spot was switched for 20 different respiratory phases, or once every 1.5 mm of motion. The transducer could potentially steer as fast as every 16 ms, if necessary.

Each phantom sonication was monitored using the described hybrid multi-baseline referenceless thermometry algorithm and multishot readout-segmented EPI pulse sequence, designed for accurately depicting the heating of the focal spot while in motion [19]. The sonications were allowed to proceed for enough time such that the central zone of the hotspot reached a temperature of at least 15°C above baseline. From this image, the following parameters were measured. First, the lengths, widths, and areas of the sonication zone that were greater than 5°C and 10°C above baseline was calculated. The temperature images were segmented at both T>5°C and T>10°C for geometric calculations. Lengths and widths were measured as the length of lines through the center of the focus; these lines were

oriented up/down for lengths and left/right for widths. The area at each temperature threshold was calculated as the number of pixels comprising each sonication region, in mm^2. Additionally, the amount of time and energy required to reach a temperature rise of 15°C at the peak were calculated. The time required to reach this temperature was measured from the time power was turned on. Finally, the temperature rise rate was calculated by using the maximum temperature measured 10 seconds into the sonication. Sonications were performed during the same session spanning over 6 hours in the following order: 5 steered, 3 unsteered, 5 static, followed by one more steered, unsteered, and static sonication. In between each sonication, at least fifteen minutes were allowed to let the phantom cool back to room temperature. Analysis of variance (ANOVA) was performed on the three groups for three measurements: the area measurements greater than 10°C, the temperature rise rate measurements, and the total energy deposited to reach 15°C above baseline measurements. Multiplicity adjusted P-values were then calculated from the Bonferroni multiple comparisons test.

In vivo HIFU Ablation

In vivo HIFU ablation experiments were performed in 6 healthy pigs. These experiments were approved by Stanford University's animal care and use committee. The pigs were sedated and mechanically ventilated at a rate of 12.5 breaths per minute, resting supine on the MRI table. The HIFU transducer was placed subcostally, so as to avoid rib heating. Ultrasound reflection tests were prescribed to verify good transducer membrane-to-skin coupling, using water to make the initial connection and then allowing the transducer's leaky membrane to maintain it. With good coupling verified, the transducer was fixed in place with velcro straps. Using the steps as outlined above, steered ablations were prescribed, using the vessels and diaphragm in a sagittal slice to track the liver motion. MR-ARFI was used for focal spot calibration, and finally, steered ablations were performed, ablating the liver at maximum transducer power of 150 acoustic Watts for varying durations. Throughout the ablations, the transducer and skin were cooled with chilled, circulating water. Breath-hold ablations were also performed, and the temperature characteristics between steered and breath-hold ablations were compared. The temperature rise rate was calculated by measuring the temperature of the ablation at 10 seconds. This time was selected to minimize perfusion effects, while also allowing time for respiratory motion to occur. For one pair of ablations located 5 mm from each other, the lengths and widths of the ablation zone that were greater than 5°C above baseline were also calculated at the time the maximum temperature rise surpassed 10°C. As not every ablation reached 10°C, due to perfusion effects, these measurements were not performed on all ablations. Statistical methods were only performed on the temperature rise rate calculations, using the Student's t-test.

Results

Phantom Experiments

Images from phantom sonications when the maximum temperature first reached 15°C above baseline are shown in Figure 5. Measured values are all provided in Table 1. Figure 6 shows the length and width measurements for each sonication type and centered for the contour of

>5°C above thermal baseline. For the >10°C contours, the areas of the unsteered, steered, and static sonications were 0.73 ± 0.19 cm^2, 0.10 ± 0.012 cm^2, and 0.075 ± 0.018 cm^2, respectively. The differences in areas between steered and unsteered and static and unsteered were statistically significant ($p < 0.0001$), but were not significant between steered and static sonications ($p > 0.9999$). Considering the total energy deposition required for each focus to achieve 15°C, compared to the static sonication, the amount of additional energy required for the steered sonication was 118 ± 159 J. For the non-steered sonication, the additional energy was 6559 ± 1790 J. For these cases, the static versus steered ablation differences were not significant ($p > 0.9999$), while both steered and static ablations were significantly different from unsteered ($p < 0.0001$). For the temperature rise rate metric, the differences between unsteered sonications and both steered and static sonications were statistically significant ($p < 0.0001$). Between static sonications and steered sonications, the difference was also significant ($p = 0.0030$).

In Vivo HIFU Ablations

Thirty-two HIFU ablations were performed *in vivo* in the porcine model. The ablation depths ranged from 64 mm to 117 mm away from the transducer face. Figure 7 shows example images from a HIFU ablation, as well as a representative ARFI-image. The temperature standard deviation in the images varied with based on position in the liver and the receive coil locations. For example, in one animal near the gall bladder the temperature standard deviation was 0.98°C, while closer to the dome of the liver this value was 1.20°C. In another pig, the temperature standard deviation was 0.67°C to 1.04°C. The reduced field of view thermometry and ARFI images are visualized as tiles on top of the larger field of view scout images. As the liver moves, the tile's position on the scout image is adjusted to reflect the change in position.

In general, most breath-hold ablations were not prescribed directly adjacent to a steered location. However, Figure 8 shows representative images of a steered ablation performed in a location 5 mm from the breath-hold location. In this case, length and width calculations similar to the phantom ablations were performed. The breath-hold ablation reached a peak temperature of 10.2°C above baseline prior to ablation end. Therefore, hot spot characteristics were measured when both sonications resulted in temperatures greater than 10°C. The steered ablation required 31.2 seconds of ablation time to reach 10°C. At this time, the dimensions of the spot at the 5°C contour was 0.67 cm (motion direction) by 0.64 cm (non-motion direction). For the breath-hold ablation, the ablation time was 26.7 seconds, with the 5°C dimensions being 0.49 cm (motion direction) by 0.58 cm (non-motion direction). In terms of energy depositions required to reach these temperatures, this breath-hold required 3953 J, compared to 4612 J (16.7% extra energy) for the steered ablation case. This difference is similar to the additional energy required for a steered ablation compared to a static ablation in the phantom model.

The maximum temperature achieved 10 seconds after each ablation began was measured to determine its initial temperature rise rate for both steered and breath-hold ablation types (Table 2). These were compared to ablations performed in muscle. Although the temperature rise rates varied greatly within the liver, the average steered temperature rise rate was 95%

of the average breath-hold rate over the same period of time. The two liver ablation groups were not significantly different ($p = 0.62$).

Discussion

The results of this work demonstrate that respiration-based beam steering is feasible, demonstrated both in phantom sonications as well as *in vivo* in the porcine model. Although our transducer was not optimal because it could not deliver enough energy at its center frequency to coagulatively necrose tissue in heavily perfused organs *in vivo*, it was a good testbed for experimenting with this focusing technique. By assuming a regular pattern of respiratory motion, external motion was measurable and could be correlated to motion in the abdomen. Our lookup table method decoupled the measurement from MR imaging, allowing us to dedicate all imaging time towards thermometry while still controlling the transducer with minimal latency. As these methods are independent, theoretically the scanner need not be active. Steering and power could be controlled even while not scanning the primary ablation region, such as when changing the MRI scan plane to monitor skin heating.

Phantom Experiments

The HIFU phantom sonication experiments demonstrated the potential for respiratory-based steering techniques. Triggering based on an external motion signal has been demonstrated to refocus HIFU energy at the desired target location. The size and energy deposition of the steered foci are very close to the static ones. The required input energy for the steered respiratory sonication was around 118 ± 159 J (12.8%) more than a static sonication. Although steered sonications had a statistically slower temperature rise rate compared to static sonications, the energy deposition and sonication area measurements were statistically indistinguishable.

The discrepancy may be explained by the fact that for a static sonication, the focus will heat a specific voxel very well compared to the steered case. The other two measurements, in this case, could be more indicative of the overall steering quality. This shows good tracking compared to both non-steered, moving and non-moving cases. It is known that when an electronically steered beam is steered off-axis, the energy lost to grating lobes increases, an effect described by Payne et al. [20] for focused ultrasound. In addition, there is a 2% loss in efficiency when switching the InSightec transducer's phases from one target location to another. Both of these factors contribute to the extra treatment time. Motion during the vessel/diaphragm step could also have decreased the accuracy of the focal targeting, particularly at the moment of maximum speed during the phantom motion; with the current sequence the sampling of the fiducial marker position could have had gaps as large a 5.6 mm at the maximum velocity phase. Acquiring these images faster or gated could help improve the targeting accuracy.

In Vivo HIFU Ablations

We also performed ablations *in vivo* in the porcine model. Like the steered HIFU phantom sonication, the steered *in vivo* ablations required slightly more energy deposition compared to the breath-hold cases. The two ablation types were not statistically significantly different

from each other, based on the temperature rise rate metric. However, the results were hampered because proximity to blood vessels can greatly change the ablation's thermal profile [21]. For example, for the muscle ablations, temperatures routinely were greater than 25°C above baseline for breath-hold ablations, while liver ablations typically only crossed 10°C over baseline before reaching steady state, using this transducer. To minimize perfusion effects, we used a metric of temperature at 10 seconds. Utilizing a shorter metric time would have further minimized perfusion effects, however there would be less overall motion to distinguish the breath-holds from steered ablations. Other factors can exist that might affect the steering quality assessment, such as potentially changing aberrations between the target and focus that could affect the intensity at the focus and reduce energy deposition. Repeating these experiments with a higher powered, higher frequency transducer might be more successful at achieving coagulative necrosis. While our transducer was useful for testing ablation and steering strategies, the energy delivered at 550 kHz could not routinely achieve a sufficient thermal dose in the liver. Gross pathology showed no thermal lesion. While out-of-plane motion should have been minimized by acquiring a sagittal plane, this could also affect the assessment of steering quality. Finally, all the considerations described in the phantom experiment discussion about off-axis steering resulting in a loss of intensity at the desired focal point are relevant here as well.

One benefit of respiration based steering using an external monitor is that this approach is independent from imaging. As a result, any slice may be monitored without also needing to monitor liver motion. The respiratory sampling rate can also be very rapid, as fast as 1 kHz, meaning very low potential latencies for HIFU steering, which are now less than the transducer's fastest switching speed.

Another benefit for *in vivo* respiration based steering is the ability to assess focal locations throughout the entire respiratory cycle before treatment. As focus locations are determined beforehand, all respiratory phase locations can be independently verified with acoustic radiation force imaging to assess the quality of focusing at the target. This could be important for trans-costal rib ablations or for targets requiring acoustic correction.

The time needed for the in vivo treatments varied. This was dependent on the breathing rate. For example, an MR-ARFI scan required two breaths to acquire an image, so acquiring MR-ARFI images across the respiratory cycle can take many minutes. Reducing the time for all of this imaging is possible. For example, perhaps fewer respiratory locations are necessary to create an accurate target map. Another option is adding the ability to guide patients in their breathing, perhaps through visual feedback mechanisms, also potentially improving the acquisition of these scans. This should also limit the potential of liver drift with respect to the respiratory belt signal. Over periods of time (e.g. 20 minutes), the liver's position can drift with respect to external signals like skin measurements (i.e. a respiratory belt) [22]. Cattin *et al*. stated that during shorter periods, 10 minutes or less, the average deviation from setup position is less than 3 mm [22]. The current ablation process takes roughly this amount of time, but speeding up the target setup time could improve this. Additionally, a hybrid method which combined these a priori lookup tables with periodic transducer and anatomical fiducial analysis to compensate for drift could further improve the safety and effectiveness of this steering technique.

While the respiratory belt was satisfactory for our phantom and liver motion experiments, in patients it could present some problems, primarily because it is an AC-coupled, secondary measure of motion. If a patient held his breath, the signal would gradually decay to zero, instead of maintaining a constant value. This could be improved by switching to other external signals that quantify liver motion. Other non AC-coupled techniques include utilizing an ultrasound transducer to track objects [23–25] or 1D speckle patterns [26,27] and monitoring respiration with a CCD camera to detect motion [28]. As long as any of these other sensors can convert into a single signal (ie a single value changing over time), they could easily be incorporated into our system.

Conclusion

We have demonstrated a system for performing HIFU steering during liver ablation. By registering a respiratory signal to that of tissue motion, we have shown the method can target liver tissue during periodic respiration. The tracking method was tested in phantom sonications and *in vivo* porcine experiments. The method has low latency, and can help reduce patient safety errors. Furthermore, while the system presented here utilized a respiratory belt signal, this signal could be replaced with any motion measurement, be it pressure, ultrasound, or optical sensors to measure motion.

Acknowledgements

The authors acknowledge Wendy Baumgartner for assistance with animal care and support, as well as Sandra Rodriguez, Kevin Epperson, and Anne Sawyer for assistance related to MRI scanning. We also acknowledge InSightec, particularly Alex Kavushansky and Omer Brokman, for technical support. Finally, we recognize our funding sources: NIH R01 CA121163 and P01 CA159992.

References

1. Chapman A, ter Haar G. Thermal ablation of uterine fibroids using MR-guided focused ultrasound-a truly non-invasive treatment modality. European Radiology. 2007; 17:2505. [PubMed: 17473924]
2. Murat FJ, Gelet A. Current status of high-intensity focused ultrasound for prostate cancer: Technology, clinical outcomes, and future. Current Urology Reports. 2008; 9:113. [PubMed: 18419995]
3. Hynynen K, Clement G, McDannold N, Vykhodtseva N, King R, White P, Vitek S, Jolesz F. 500-element ultrasound phased array system for noninvasive focal surgery of the brain: A preliminary rabbit study with ex vivo human skulls. Magn. Reson. Med. 2004; 52:100. [PubMed: 15236372]
4. Martin E, Jeanmonod D, Morel A, Zadicario E, Werner B. High-intensity focused ultrasound for noninvasive functional neurosurgery. Annals of Neurology. 2009; 66:858. [PubMed: 20033983]
5. Gianfelice D, Gupta C, Kucharczyk W, Bret P, Havill D, Clemons M. Palliative treatment of painful bone metastases with MR imaging–guided focused ultrasound. Radiology. 2008; 249:355. [PubMed: 18695209]
6. Xiong L, Hwang J, Huang X, Yao S, He C, Ge X, Ge H, Wang X. Early clinical experience using high intensity focused ultrasound for palliation of inoperable pancreatic cancer. J. Pancreas. 2009; 10:123.
7. Gedroyc W. New clinical applications of magnetic resonance-guided focused ultrasound. Topics in Magnetic Resonance Imaging. 2006; 17:189. [PubMed: 17414076]
8. Illing R, Kennedy J, Wu F, ter Haar G, Protheroe A, Friend P, Gleeson F, Cranston D, Phillips R, Middleton M. The safety and feasibility of extracorporeal high-intensity focused ultrasound (HIFU) for the treatment of liver and kidney tumours in a Western population. Br. J. Cancer. 2005; 93:890. [PubMed: 16189519]

9. de Senneville B, Mougenot C, Moonen C. Real-time adaptive methods for treatment of mobile organs by MRI-controlled high-intensity focused ultrasound. Magn. Reson. Med. 2007; 57:319. [PubMed: 17260361]
10. Kokuryo, D.; Kaihara, T.; Kumamoto, E.; Fujii, S.; Kuroda, K. Method for target tracking in focused ultrasound surgery of liver using magnetic resonance filtered venography. Engineering in Medicine and Biology Society, 2007. EMBS 2007; 29th Annual International Conference of the IEEE; 2007. p. 2614
11. de Senneville B, Noe K, Ries M, Pedersen M, Moonen C, Sorensen T. An optimised multi-baseline approach for on-line MR-temperature monitoring on commodity graphics hardware. IEEE International Symposium on Biomedical Imaging: From Nano to Macro. 2008; 5:1513.
12. Quesson B, Laurent C, Maclair G, de Senneville B, Mougenot C, Ries M, Carteret T, Rullier A, Moonen C. Real-time volumetric MRI thermometry of focused ultrasound ablation *in vivo*: a feasibility study in pig liver and kidney. NMR in Biomedicine. 2011; 24:145. [PubMed: 21344531]
13. Auboiroux V, Viallon M, Roland J, Hyacinthe J, Petrusca L, Morel D, Goget T, Ter-raz S, Gross P, Becker C, et al. ARFI-prepared MRgHIFU in liver: Simultaneous mapping of ARFI-displacement and temperature elevation, using a fast GRE-EPI sequence. Magnetic Resonance in Medicine. 2012:932. [PubMed: 22246646]
14. Santos J, Wright G, Pauly J. Flexible real-time magnetic resonance imaging framework. Conf. Proc. IEEE Eng. Med. Biol. Soc. 2004; 2:1048. [PubMed: 17271862]
15. Dumoulin C, Mallozzi R, Darrow R, Schmidt E. Phase-field dithering for active catheter tracking. Magn. Reson. Med. 2010; 63:1398. [PubMed: 20432311]
16. Korin H, Ehman R, Riederer S, Felmlee J, Grimm R. Respiratory kinematics of the upper abdominal organs: a quantitative study. Magnetic resonance in medicine. 1992; 23:172. [PubMed: 1531152]
17. Holbrook A, Ghanouni P, Santos J, Medan Y, Pauly K. In vivo MR acoustic radiation force imaging in the porcine liver. Medical Physics. 2011; 38:5081. [PubMed: 21978053]
18. Grissom W, Rieke V, Holbrook A, Medan Y, Lustig M, Santos J, McConnell M, Butts Pauly K. Hybrid referenceless and multibaseline subtraction MR thermometry for monitoring thermal therapies in moving organs. Medical Physics. 2010; 37:5014. [PubMed: 20964221]
19. Holbrook A, Santos J, Kaye E, Rieke V, Butts Pauly K. Real-time MR thermometry for monitoring HIFU ablations of the liver. Magn. Reson. Med. 2010; 63:365. [PubMed: 19950255]
20. Payne A, Vyas U, Todd N, de Bever J, Christensen D, Parker D. The effect of electronically steering a phased array ultrasound transducer on near-field tissue heating. Medical Physics. 2011; 38:4971. [PubMed: 21978041]
21. Dasgupta S, Banerjee R, Hariharan P, Myers M. Beam localization in HIFU temperature measurements using thermocouples, with application to cooling by large blood vessels. Ultrasonics. 2010:171. [PubMed: 20817250]
22. von Siebenthal M, Sźekely G, Lomax A, Cattin P. Systematic errors in respiratory gating due to intrafraction deformations of the liver. Medical Physics. 2007; 34:3620. [PubMed: 17926966]
23. Auboiroux V, Petrusca L, Viallon M, Goget T, Becker C, Salomir R. Ultrasonography-based 2D motion-compensated HIFU sonication integrated with reference-free MR temperature monitoring: a feasibility study *ex vivo*. Physics in Medicine and Biology. 2012; 57:N159. [PubMed: 22517112]
24. Tanter M, Pernot M, Aubry J, Montaldo G, Marquet F, Fink M. Compensating for bone interfaces and respiratory motion in high-intensity focused ultrasound. International Journal of Hyperthermia. 2007; 23:141. [PubMed: 17578338]
25. Marquet F, Aubry J, Pernot M, Fink M, Tanter M. Optimal transcostal high-intensity focused ultrasound with combined real-time 3D movement tracking and correction. Physics in Medicine and Biology. 2011; 56:7061. [PubMed: 22016152]
26. Petruca, L.; Arnold, P.; Goget, T.; Celicanin, Z.; Auboiroux, V.; Viallon, M.; Santini, F.; De Luca, V.; Terraz, S.; Tanner, C.; Scheffler, K.; Becker, C.; Cattin, P.; Salomir, R. Simultaneous ultrasound/MRI motion monitoring in the abdomen; Proceedings 8th Interventional MRI Symposium; 2010. p. 153

27. Schwartz B, McDannold N. MRI motion compensation by positional ultrasound biometrics. Proc. Intl. Soc. Mag. Reson. Med. 2011; 19:3721.

28. Hsu, MC.; Chang, H.; Chen, YY.; Lin, WL. High intensity focused ultrasound thermal therapy for liver tumor with respiration motion; Proc. IEEE Ultrasonics Symposium; 2006. p. 1734

Figure 1. Liver Ablation Software Interface

Images are primarily displayed in the center of the user interface, and can have various overlays, such as the optimum treatment location for the current transducer location (blue shapes), relative location of other slices (blue line in right image), and real time reduced FOV images with temperature information (red tile in left image). The real time image could be adjusted on the main scout image to more rapidly image that area of anatomy. Both HIFU and MRI control are integrated into the UI.

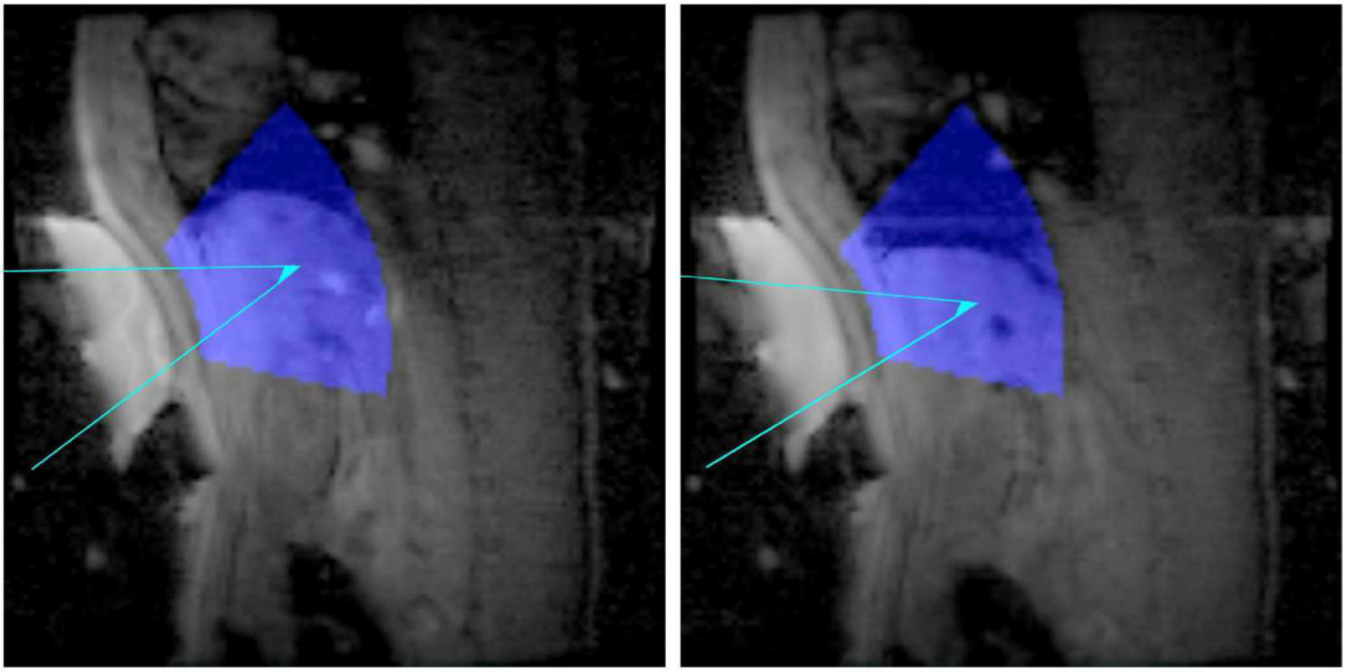

Figure 2. Transducer Tracking

The tracking coil information, besides determining the location of the transducer coil elements, was also used to visualize potential treatment areas on top of collected scout scans. The areas depicted in blue superimposed on collected scout images show regions that are 5–15 cm from the transducer face, up to an angle of 30 degrees off-axis. The aqua lines depict a target steering path to a focus in the liver from the transducer at two locations of the respiratory cycle.

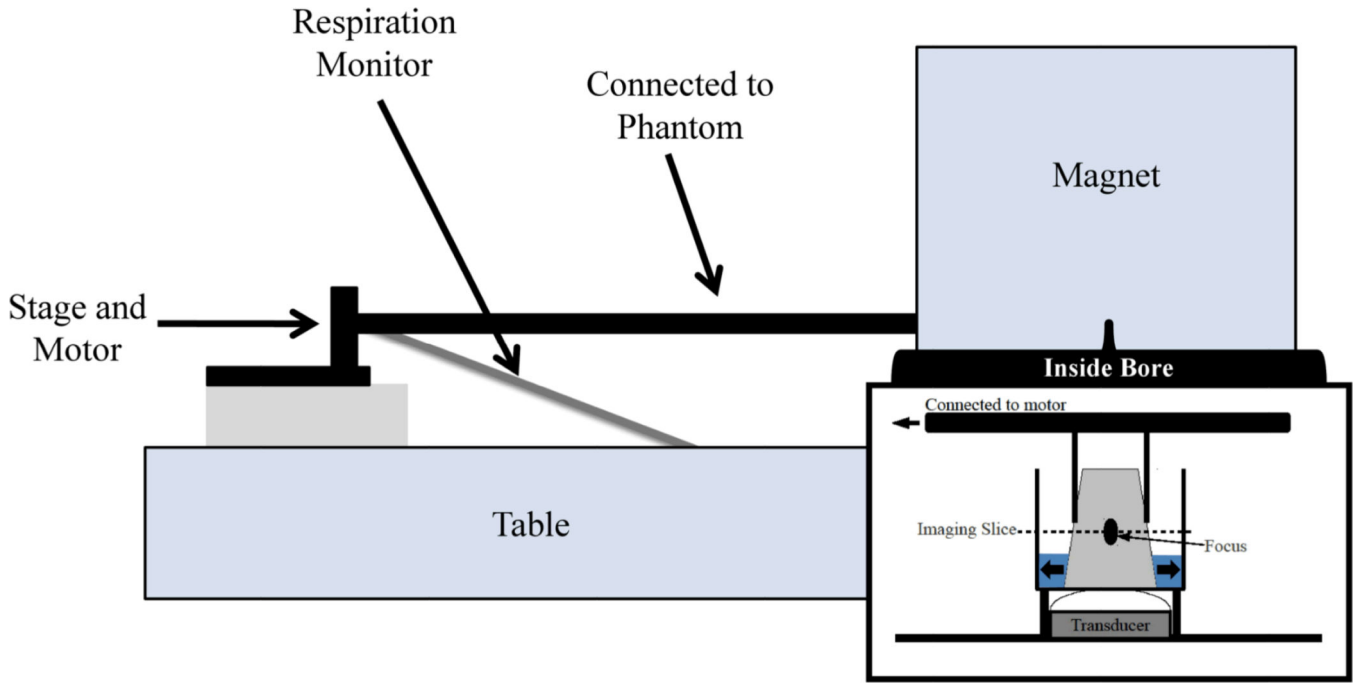

Figure 3. Phantom Experimental Setup

A rod is connected on one end to a stage that is moved back and forth with a servomotor and on the other end to the phantom within the magnet bore. The scanner respiratory belt is attached to the stage and at the other end to a fixed position on the table. As the stage moves back and forth, the respiratory belt lengthens and shortens, simulating respiratory motion.

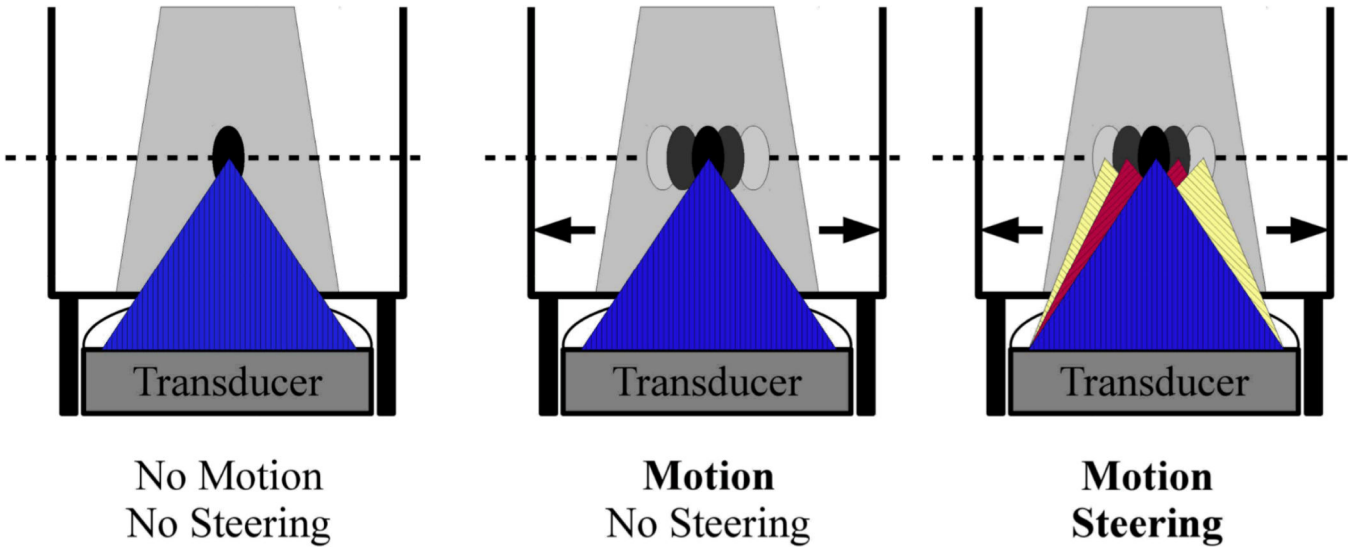

Figure 4. Sonication Types

Three types of HIFU phantom sonication experiments were performed. The first was a purely stationary sonication (left), with no phantom motion and no HIFU focal steering. The second experiment (middle) involved the phantom moving back and forth, as described in Figure 3. However, in this case the HIFU focus remains fixed in space, and thus not at a constant position in the phantom. The final experiment (right) similarly involved the phantom moving back and forth, but additionally with the system tracking this motion and steering the HIFU focus accordingly to maintain a fixed position in the phantom.

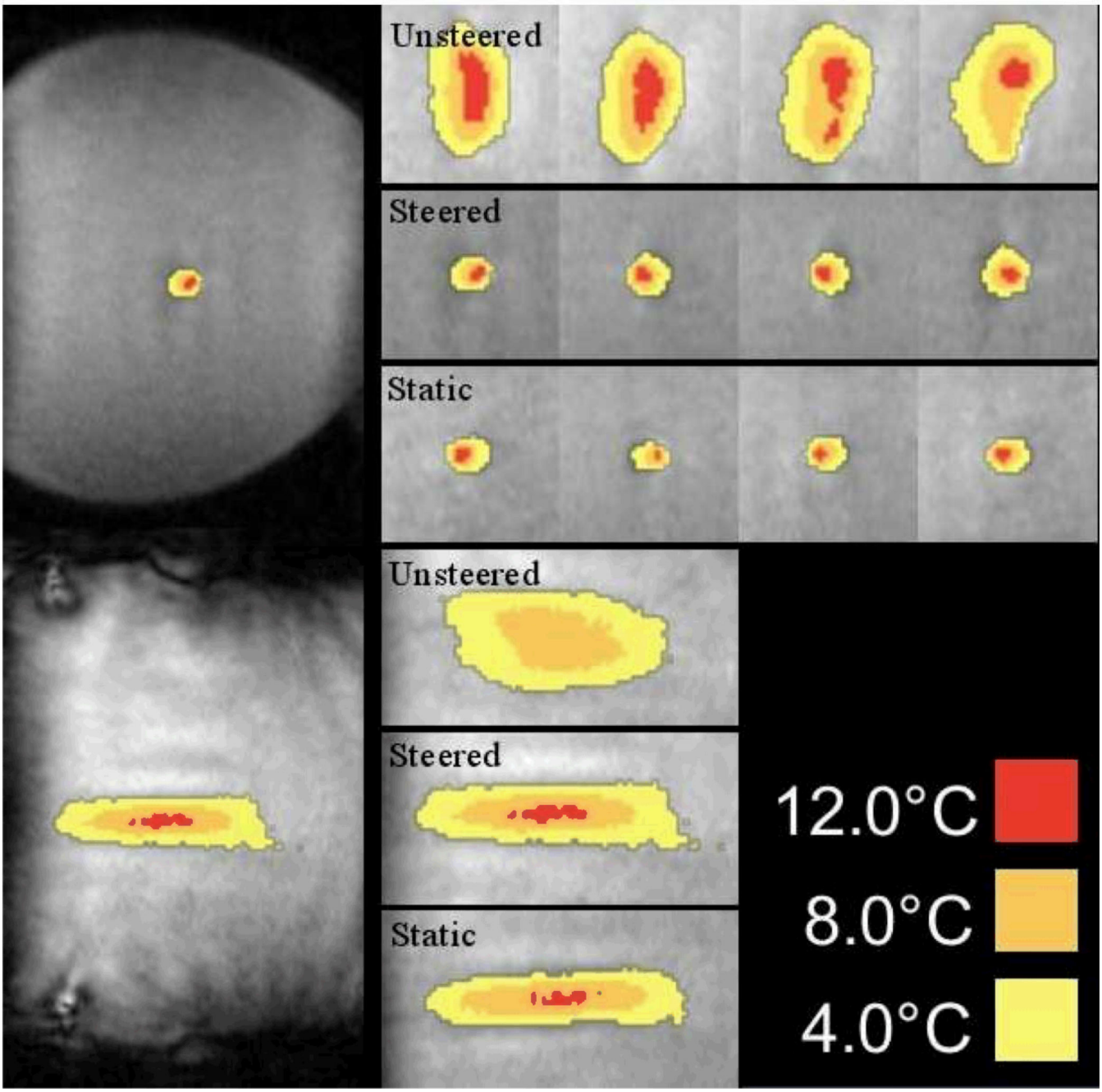

Figure 5. Phantom Sonication Images

The following real time images show representative sonication images when the focus region reached a temperature of 15°C above baseline. The left most images show the entire phantom in the reduced field of view images (8 cm × 12 cm) for steered sonication cases. The other images are representative sonications for each of the three types: unsteered sonications (1st row), steered sonications (2nd row), and static sonications (3rd row). The bottom three images show representative unsteered (4th row), steered (5th row), and static (6th row) sonications in the direction parallel to the transducer in separate experiments. The steered sonications are very similar to the static sonications.

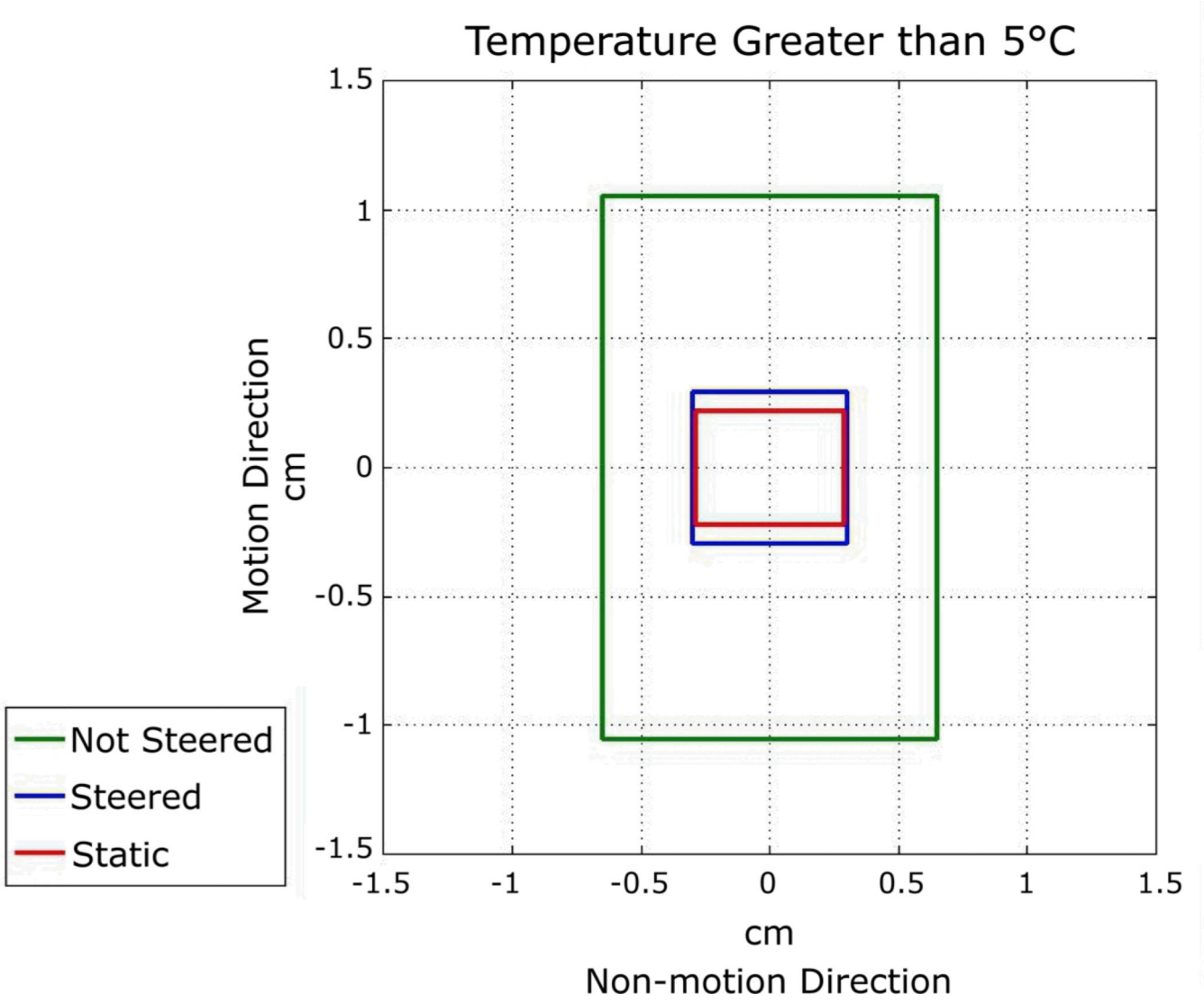

Figure 6. Phantom Sonication Spot Size Comparison

The plot shows the general dimensions of the hotspots. These measurements were made in the images acquired perpendicular to the beam (top row of images of Figure 5). The measurements are for contours of 5°C temperature rise along the motion direction (up-down) and non-motion direction (left-right) for each of three sonication types: non-steered, steered, and static sonications. Steered sonication sizes are very close to static sonications. See Table 1 for more phantom sonication characteristic details. The difference in hotspot size in the non-motion direction is most likely explained by heat dispersion from the focus over the longer sonication duration.

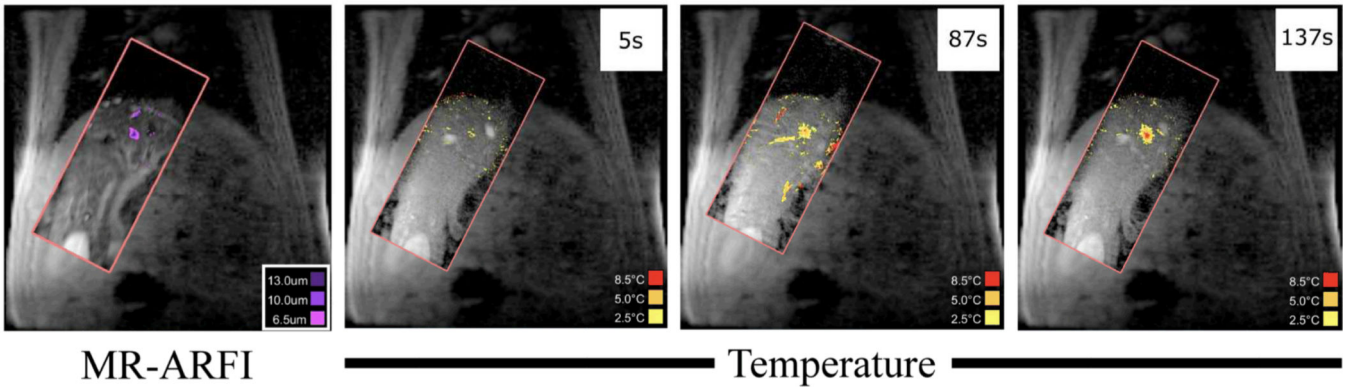

Figure 7. ARFI and Thermometry

The right three images show images of a liver ablation throughout its timecourse (the times since the beginning of the ablation are shown in white boxes). This is compared to a gated MR-ARFI verification image acquired prior to treatment (left). The rFOV images are displayed on top of the larger field of view images to provide additional anatomical context.

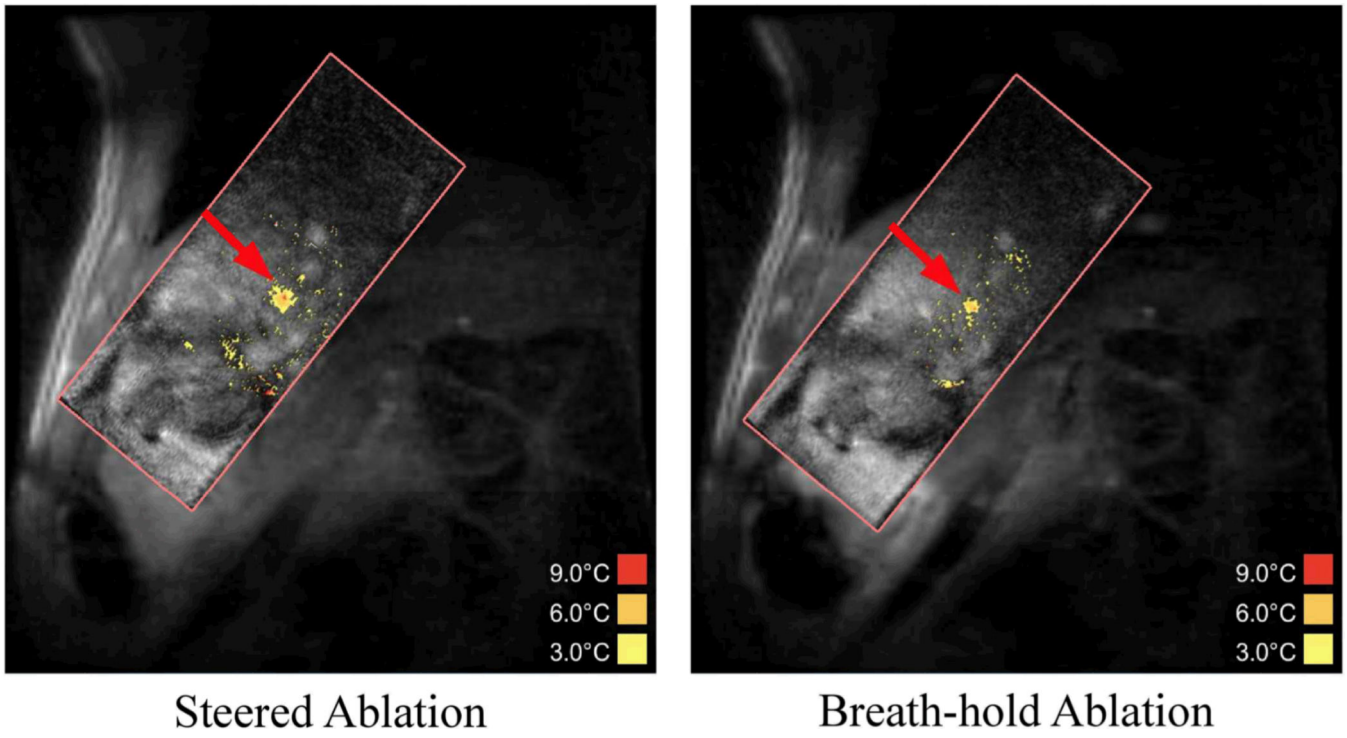

Figure 8. ***In vivo*** **HIFU Steered and Breath-hold Ablations**

These two images show representative images of a steered (left) and breath-hold (right) ablation *in vivo* at the time point when the maximum temperature reached 10°C above baseline. The steered ablation took 31.2 seconds to reach this point, while the breath-hold ablation took 26.7 seconds. The steered ablation required 16.7% more energy than the breath-hold case.

Table 1

Phantom experiments: sonication characteristics and results. The power was fixed and sonication proceeded until a temperature rise of 15°C above baseline temperature was achieved. Average measurements of the 5°C and 10°C contours are given. In addition, the temperature rise rate is calculated over the initial 10 seconds after ultrasound is turned on for each of the three conditions. In these experiments, on average, the steered temperature rise rate is 83.5% of that measured from the static condition.

Type	Not Steered	Steered	Static
Number Sonications	4	6	6
Sonication Power (W)	74.0	74.0	74.0
Length >5°C (cm)	2.11 ± 0.15	0.59 ± 0.06	0.44 ± 0.07
Width >5°C (cm)	1.30 ± 0.11	0.61 ± 0.03	0.57 ± 0.06
Area >5°C (cm^2)	2.05 ± 0.10	0.33 ± 0.03	0.26 ± 0.03
Length >10°C (cm)	1.38 ± 0.35	0.30 ± 0.06	0.24 ± 0.06
Width >10°C (cm)	0.60 ± 0.03	0.35 ± 0.04	0.28 ± 0.08
Area >10°C (cm^2)	0.73 ± 0.19	0.10 ± 0.012	0.075 ± 0.018
Sonication Time (sec)	101 ± 24	14.0 ± 1.3	12.4 ± 1.7
Energy (J)	7480 ± 1787	1039 ± 99	921 ± 125
Temperature Rise Rate (°*C*/sec)	0.51 ± 0.05	1.15 ± 0.14	1.38 ± 0.05

Table 2

In vivo porcine experiments: sonication characteristics and results. The temperature rise rate was calculated as the temperature rise per second over the first 10 second interval after ultrasound was turned on. The temperature rise rate for the steered condition was 95% that of the breathhold sonications, while both were substantially lower than that obtained in muscle tissue. For each ablation, the ablation power was 150 acoustic W, applied for 10 seconds (1.5 kJ).

Type	Steered Liver	Breath-hold Liver	Breath-hold Muscle
Number of Ablations	15	14	3
Temperature Rise Rate (°C/sec)	0.57 ± 0.13	0.60 ± 0.18	1.19 ± 0.15